

Three-dimensional optical billiard chaotic scattering

David Sweet^a, Benjamin W. Zeff^a, Edward Ott^{a,b}, Daniel P. Lathrop^{a,*}

^a Department of Physics, Institute for Plasma Research, University of Maryland, College Park, MD 20742, USA

^b Department of Electrical Engineering, Institute for Plasma Research, University of Maryland, College Park, MD 20742, USA

Received 15 September 2000; accepted 6 January 2001

Communicated by R.P. Behringer

Abstract

We report on the first experimental measurements taken from an easily studied, visually remarkable chaotic scattering system that we call an *optical billiard*. In particular, we measure the fractal dimension of the basin boundaries generated by the reflection of light from various configurations of polished, reflecting spheres. We find that our experimentally determined fractal dimension values agree well with the values we find from simulations. We also find that depending on the configuration of the spheres, the boundary can be either a nowhere-differentiable surface or else can possess the topological Wada property whereby any basin boundary point is simultaneously on the boundary of four distinct basins. Other configurations yielding other topologies of the chaotic scattering set are suggested for future study. © 2001 Published by Elsevier Science B.V.

Keywords: Optical billiard; Basin boundary; Wada property

1. Introduction

Chaotic scattering theory may be employed in the understanding of various physical systems such as those studied in chemical kinetics [1], celestial mechanics [2], cosmology [3,4], and fluid mechanics [5]. We discuss a chaotic scattering system that is useful in that it can be conveniently studied theoretically [6,7] and, as shown here, experimentally.

There are many chaotic scattering situations wherein a scattered orbit may leave the scattering region in different identifiable ways. In such cases, we call the collection of initial conditions whose subsequent orbits exit the scattering region in the same way as the *basin* for that type of exit. Numerical studies of

chaotic scattering systems reveal that the sets in state space separating such basins, called basin boundaries, can be fractal [8,9]. Fractal basin boundaries also occur in dissipative chaotic systems [8,9].

The experimental study of basin boundaries has proven difficult because these sets are non-attracting, typical initial conditions near these sets lead to orbits which tend towards regions of state space far from the basin boundaries, spending only a short time near the boundaries. One method of studying basin boundaries is to set an initial condition, run the experiment to see to which basin the initial condition belongs and repeat for many different initial conditions, thus mapping out some portion of state space showing where the basins and their boundaries lie. While this procedure has proven to be very effective when applied to computer simulations [8,9], it presents several problems when one attempts to apply it to a physical system. These problems include the accurate

* Corresponding author. Tel.: +1-301-405-1594; fax: +1-301-405-1670.

E-mail addresses: dpl@complex.umd.edu, dpl@complex.physics.umd.edu (D.P. Lathrop).

determination and placement of many initial conditions, long times associated with a very large number of experimental runs needed to map out the basins, and parameter drift over the course of many runs. Thus, fractal basin boundaries have been rarely studied experimentally. Two exceptions are Refs. [10,11]. In Ref. [10], the basin boundary for an experimental dissipative mechanical system with two basins of attraction was mapped. In Ref. [11], the basins of attraction for coupled chaotic oscillator circuits were studied.

As proposed in [12,13], we study systems, one of which was initially described in [7], which readily reveal their basins and basin boundaries to the naked eye. These systems, which we call optical billiards, consist of polished, reflective surfaces (in the cases studied here, surfaces of spheres). Relative to the previously discussed method of basin boundary study (viz., repeating many successive experiments with different initial conditions), the optical method (described subsequently) is akin to a massively parallel approach wherein each ray contributing to an image plays the role of one of the successively repeated experiments in the other method. The configurations we have studied are shown in Fig. 1. In the configuration shown in Fig. 1a each of the spheres of radius d is in contact with two neighbors, but is not in contact with the other sphere. The distance between the centers of the touching sphere is d , while the distance between non-touching spheres is l ($d < l < \sqrt{2}d$). In the configuration shown in Fig. 1b, all spheres touch ($l = d$), and the centers of the four spheres are at the vertices of a regular tetrahedron. These optical billiards have proven easy to manipulate and observe in various configurations. A configuration similar to that shown in Fig. 1b has been proposed as a device for distributing infrared networking signals [14].

We measure the fractal dimension (defined below) of the basin boundaries of five differently configured optical billiards by analyzing the digital images of these billiards. The results compare well to calculations of the fractal dimension taken from simulation data, as shown in Fig. 2. The five configurations that we study and that are plotted in Fig. 2 are (1) $l =$

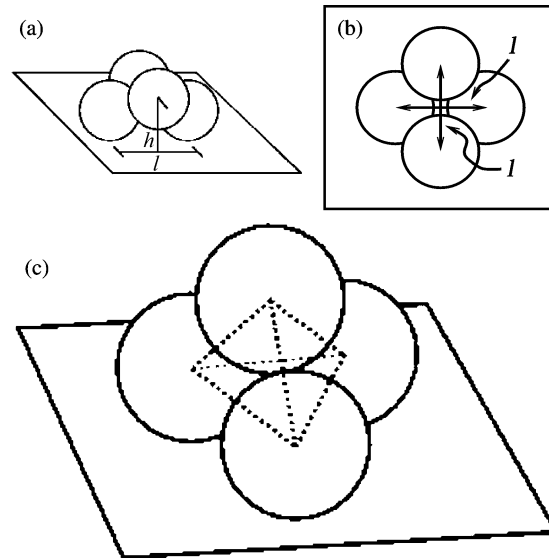


Fig. 1. Schematic of configurations of spheres used in this experiment. (a) l , the distance between opposing spheres, ranges from $l = \sqrt{2}d$ (configuration 1), where d is the diameter of a sphere, when the balls lie flat on the table to $l = d$ (configuration 5), when the balls are all touching (c). (In (c) the scatterer of (a) with $l = d$ is reoriented so that three of the spheres sit on a horizontal surface.) (b) Top view of (a).

$\sqrt{2}d$ (for which the centers of the four spheres are at the corners of a $d \times d$ square); (2) $l = 1.32d$; (3) $l = 1.22d$; (4) $l = 1.16d$; and (5) $l = d$ (for which the sphere centers form a regular tetrahedron and all spheres touch).

In addition, we note that the basin boundaries seen in configurations 1–4 exhibit a different topology than the one seen in configuration 5. The basin boundary in configurations 1–4 is a continuous surface. For configurations 2–4 we claim that this surface is nowhere-differentiable and fractal (consistent with this claim, in the two-dimensional sections seen in the images in Figs. 4–6, the basin boundary appears to be a continuous, nowhere-differentiable curve). In configuration 5, the boundary appears more complex with the four basins intertwined on an arbitrarily fine scale. In fact, as shown in [7], these basins possess the Wada property [15] whereby in any arbitrarily small neighborhood of a boundary point, there exist points in all four basins [7].

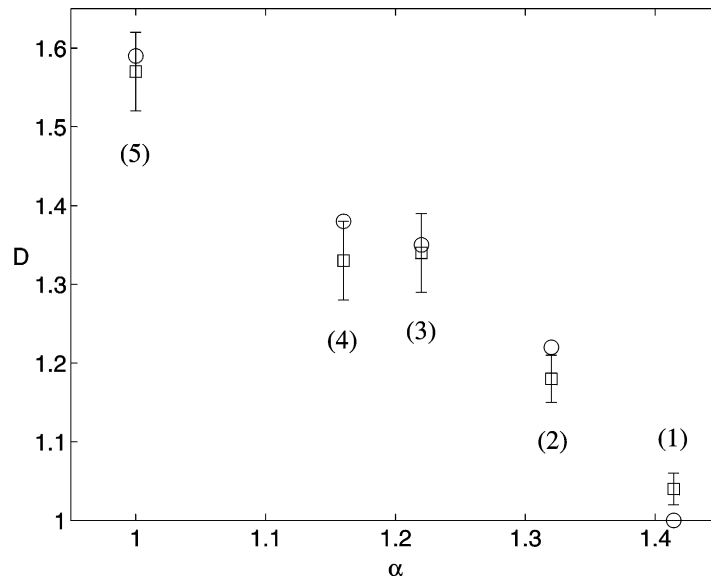


Fig. 2. Fractal dimension vs. $\alpha \equiv \ell/d$. Each value of ℓ/d represents one configuration. The points are ordered and labeled from configuration 5 at $\alpha = 1$ to configuration 1 at $\alpha = \sqrt{2}$. The squares are experimentally measured values and the circles are taken from computer simulation. The dimension values are measurements of the dimension of the basin boundaries in Figs. 3–7, which are two-dimensional slices of the full four-dimensional state space of the system.

2. Background

A three-dimensional optical billiard can be considered as a four-dimensional discrete time dynamical system mapping a four-dimensional vector describing an incident ray at the n th reflection from the scatterer to the $(n + 1)$ th reflection. Here the four-component state vector specifies the position (two components) at which a light ray hits the surface of a sphere and the orientation (two components) of the light ray as it hits the surface. The time evolution is specified by the rule that the angle of reflection from the surface is equal to the angle of incidence, where both angles are taken with respect to the surface normal (i.e., the reflection is specular), and, when the reflection is not normal to the surface, the incident and reflection direction vectors span a plane.

We define the fractal dimension (more specifically, the box-counting dimension, also called the capacity) of a set as follows. We cover the set with a grid of d_S -dimensional hypercubes having diameter ε , where d_S is the dimension of the space in which the set in question is embedded. Calling the number of these

ε -sized hypercubes which contain points in the set $N(\varepsilon)$, we define the fractal dimension, D , by the small ε scaling of $N(\varepsilon)$,

$$N(\varepsilon) \sim \varepsilon^{-D} \quad (1)$$

A strict definition of fractal dimension would require this scaling to persist down to arbitrarily small ε (i.e., $D = \lim_{\varepsilon \rightarrow 0} [\ln N(\varepsilon)] / [\ln(1/\varepsilon)]$), but we will use the term fractal dimension when referring to analyses of our experimental data even though the scaling (1) is necessarily cut off at some minimum length scale, ε_{\min} .

Our basin boundaries divide the four-dimensional state space into different regions (the basins) and hence must be at least three-dimensional. They can, however, be intricately wrinkled and folded so that their fractal dimension is a non-integer between 3 and 4.

Note that since the pictures in Figs. 3–7 represent a two-dimensional slice of a four-dimensional state space, the assumption that the intersection of this slice with the basin boundary is generic implies that the fractal dimension of the basin boundary in

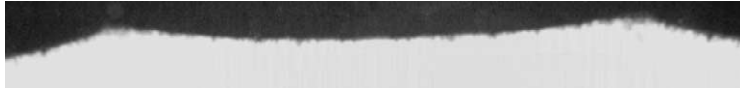


Fig. 3. Image of the system in configuration 1. The image was acquired in color but was converted to grayscale by the transformation $(R', G', B') = [\frac{1}{3}(R + G + B)](1, 1, 1)$ for subsequent analysis. The image size is (width \times height) 1284 pixels \times 150 pixels.



Fig. 4. Image of the system in configuration 2. The image size is 836 pixels \times 374 pixels.



Fig. 5. Image of the system in configuration 3. The image size is 2415 pixels \times 945 pixels.



Fig. 6. Image of the system in configuration 4. The image size is 1773 pixels \times 927 pixels.

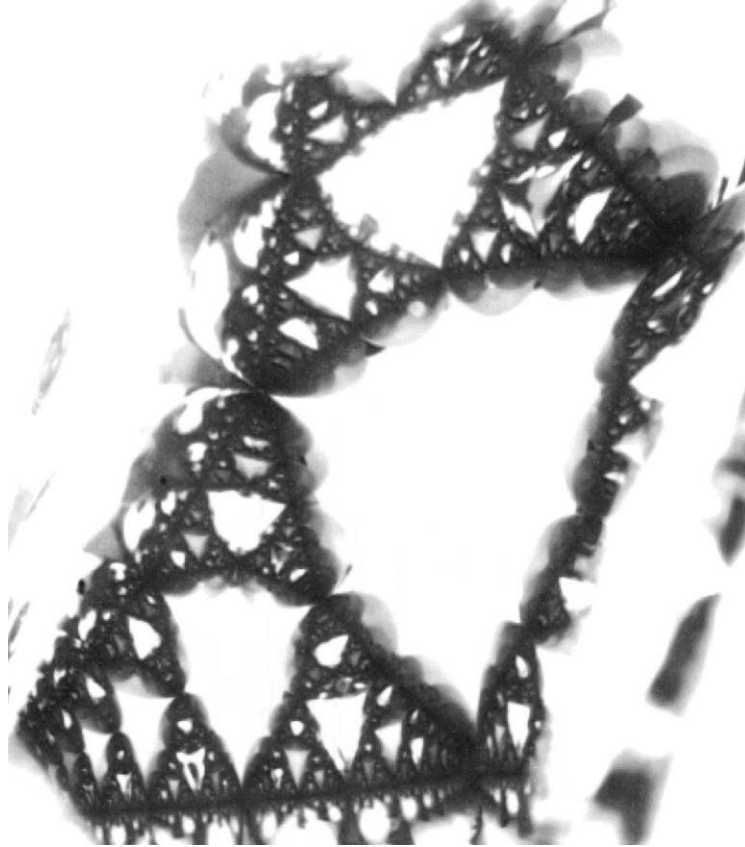


Fig. 7. Image of the system in configuration 5. The image size is 754 pixels \times 857 pixels.

the full state space is equal to 2 plus the fractal dimension of the portion of the boundary contained in the slice. Throughout, when we will refer to the dimension of the boundaries we will be referring to the dimension as measured in such a two-dimensional slice.

We can define a scattering region for our billiard scatterers in Fig. 1 as the region that is within the tetrahedron whose edges connect the sphere centers but outside the spheres. Note that for Fig. 1c the tetrahedron is regular and none of its edges are in the scattering region, while for Fig. 1a the two edges which connect opposing spheres are on the boundary of the scattering region. (We also consider the special case $\ell = \sqrt{2}d$ (configuration 1) for which the sphere centers are coplanar and the tetrahedron degenerates to a two-dimensional square $d \times d$ surface.) All orbits that

are bounded for all forward and backward time ($t \rightarrow \pm\infty$) are contained within the scattering region. The set of all these bounded orbits is ergodic and forms what we shall refer to as the chaotic invariant set for our scatterer. If an orbit enters the scattering region and then leaves it, it never returns. A ray entering the scattering region has multiple ways to exit. In particular, there are four exits for the configuration in Fig. 1b corresponding to exits through the four faces of the regular tetrahedron, while for Fig. 1a there are two exits. (In the latter case we can define the instant at which the orbit exits upward (downward) as occurring when an orbit leaves the scattering region by crossing one of the two upper (lower) triangular tetrahedron faces.)

When one views the billiard, one sees images of objects outside the exits, generally reflected multiple

times before reaching the viewer's eye. For definiteness, suppose that there is a red piece of paper just outside one of the exits. The basins in this system can be understood by imagining this system in *reverse time*. Thus, one sees that each image of the red paper on the surface of the billiard combined with the angle at which the system is being viewed is a collection of initial light ray conditions that will be reflected by the billiard (in reverse time), eventually exiting and reaching the red paper. More directly, one could aim a narrow light beam, e.g., from a laser pointer, at a reflected image of the red paper in one of the spheres and note that the light hits the red paper. In dynamical system terms, the initial condition defined by a point on the scatterer surface in the image of the red paper and the direction given by the line between this point and the tip of the laser pointer lies in the basin of initial conditions which escape through the red paper exit. An image of the billiard in Fig. 1b showing portions of all four basins via reflections of colored paper is given in [7], where the Wada property (see Section 1) of this basin boundary is discussed.

The basin boundaries found in configurations 1–4 have a different topology from the one in configuration 5. The basin boundary in configurations 1–4 divides the state space into basins of the two exit modes: upward escape and downward escape. That is, light rays interacting with the billiard may exit the system upward or downward. The boundary is a continuous surface. (Here we call a set in the four-dimensional state space a continuous surface if it is topologically conjugate to a three-dimensional manifold, i.e., there is a *continuous*, invertible correspondence between points in the set and points in a three-dimensional manifold.) Since we find that this surface is fractal in configurations 2–4, we conclude that the surface is nowhere-differentiable in these cases [9,12,13]. Figs. 3–6 show a two-dimensional slice through the four-dimensional state space that intersects the boundary on a curve which, for Figs. 4–6 (configurations 2–4), appears to be nowhere differentiable. In contrast, the state space of the system in configuration 5 contains four basins, and the intersection of a two-dimensional state space slice with the basin boundary is not a curve (see Fig. 7). (A set is

a closed curve if it is topologically conjugate to the unit circle.)

In studies of chaotic scattering systems, points lying in the basin boundary are typically part of the stable manifold of a chaotic saddle. A chaotic saddle is a non-attracting, ergodic, chaotic set, invariant under forward and backward system evolution. (For example, in the case of Fig. 1, the chaotic saddle is contained within the tetrahedron formed by the sphere centers.) The stable manifold of the chaotic saddle is the set of initial conditions that asymptote to the chaotic saddle on forward time evolution and thus never leave the scatterer. Initial conditions near, but not precisely on, the stable manifold generate orbits that spend a long time near the chaotic saddle before leaving the scatterer. Typical initial conditions on the chaotic saddle behave chaotically, typical initial conditions near the chaotic saddle experience transient chaotic motion before exiting the scatterer. The basin boundaries we study here appear to be stable manifolds of chaotic saddles because numerical studies show that the number of bounces a light ray experiences before escaping the scatterer increases as we get closer to the basin boundary. Experimental evidence is discussed in Section 4.

3. Apparatus

The configurations were constructed with a set of four polished, reflective spheres. Images were captured with a digital camera and analyzed using custom image analysis software.

The spheres used in these experiments were AISI E52100 (chrome alloy). The camera was a Kodak DCS-460 having 3000×2000 pixel resolution. Pictures were taken with a 200 mm lens at $f/11$ or $f/22$ and both +1 and +4 diopters affixed to the end of the lens. Because the scattering surfaces are curved, light incident upon them spreads with each reflection, resulting in large variations in focal distance within the image. Due to this spreading and the three-dimensional nature of the scattering system, depth-of-field was problematic and, consequently, only a portion of the image was properly focused. Images were cropped to the in-focus portion as the first step in the data analysis, and these

cropped portions contained from roughly 2×10^5 to 2×10^6 pixels.

Each pixel in the resulting images is described by a *RGB triple* of 8 bit integers (R, G, B), which describes, respectively, the proportion of red, green, or blue in the pixel.

The light source used when photographing configurations 1–4 was a 300 W incandescent bulb mounted inside an overhead projector. Three 60 W incandescent bulbs were used to light configuration 5.

4. Methods

Each of the configurations in Fig. 1 can be described by a parameter, $\alpha \equiv \ell/d$, where ℓ is the distance between the centers of opposing balls, $1 < \alpha \equiv \ell/d < \sqrt{2}$, and d is the diameter of a ball, $d = 7.62$ cm. When $\alpha = \sqrt{2}$, the centers of the balls all lie in the same plane so that each sphere is touching its two neighbors and the centers of the spheres lie at the vertices of a square. When $\alpha = 1$, opposing spheres are touching which means that each sphere is touching all of the other three. In this case the centers of the spheres lie at the vertices of a regular tetrahedron. In the other three configurations, α is between 1 and $\sqrt{2}$, each sphere is touching only two others, but the sphere centers do not lie in a plane. The balls were positioned by first placing two balls on a flat surface a distance ℓ apart, then placing the other two balls on stands having height $\sqrt{d^2 - \frac{1}{2}\ell^2}$.

Two different photographic methods were used in this experiment. The first method was applied to configurations 1–4 and the second to configuration 5. In the first method the system was illuminated from below through the opening between the four spheres. By imaging the surface of a sphere from a particular camera location we are fixing two of the state space variables — the two angle variables — and, in effect, making a two-dimensional slice of the state space. This picture shows bright regions, corresponding to rays originating from the light shone through the opening between the spheres (the “light basin”) and dark regions, corresponding to unilluminated ray paths that do not originate from below the opening (the “dark basin”). The boundary between light and

dark basins in this slice is taken to be the basin boundary. In the second method, light was shone in through all four openings so that all points on the surfaces of the spheres that were lying in basins were illuminated. This leaves the basin boundary dark. (As discussed below, regions near the boundary are also dark.)

To implement the first method we placed the spheres on top of a clear piece of glass mounted over a light (i.e., the surface of an overhead projector where the transparencies are normally placed). Between the glass and the spheres we placed a sheet of white paper to eliminate direct reflections of the bulb off the spheres, thus providing a more even light source. Figs. 3–6 show a set of photographs resulting from this procedure. These photographs were taken with an f -stop of $f/11$ and a 3 s exposure time.

Notice that the transition from the light region to the dark region in Figs. 3–6 is not sharp, consistent with the hypothesis that the basin boundary is the stable manifold of a chaotic saddle. Light rays creating the camera image at these points have been reflected multiple times from the spheres. At each reflection a beam of rays experiences absorption and spreading with both effects leading to decreased intensity of the light. In fact, the image grows darker as we approach the boundary, indicating that it requires more and more bounces for a light ray to escape the scatterer as it comes closer and closer to the basin boundary.

Since the image grows darker as we look closer to the basin boundary, we would expect that if the scatterer were lit uniformly from all directions that the boundary would appear dark and the basins light. Indeed they do, and we used this technique for configuration 5. The uniform lighting is provided by keeping the camera shutter open for 10 s and slowly waving four incandescent light bulbs around the scatterer using an aperture of $f/22$. Fig. 7 shows the image of configuration 5 used in the data analysis.

5. Analysis

5.1. Analysis of experimental data

The method for analyzing the data in Figs. 3–7 was to identify bright and dark regions and use

box-counting (Eq. (1)) to estimate the fractal dimension of the boundary between them, i.e., the basin boundary.

Ideally, the bright and dark regions in Figs. 3–6 could be distinguished and thus one could identify the boundary. Similarly, identifying the bright regions in Fig. 7 would distinguish the four basins from the basin boundary. These ideal scenarios are compromised by effects such as the soft transition to the basin boundary discussed in Section 4 and below.

Practically, bright regions are identified via *thresholding*: each point in the image is tested to see whether its intensity (defined as $I = \frac{1}{3}(R + G + B)$) is greater than some value T , where $0 \leq T \leq 255$. The pixel is replaced with the triple $(0, 0, 0)$ — black — if $I < T$ or $(255, 255, 255)$ — white — if $I \geq T$. The appropriate value of T could not be chosen a priori, so the scaling (1) was checked for the entire range of T (at every twelfth integer value).

Edges were traced (or “detected”) in the thresholded images (in which each pixel is either black or white) by declaring a pixel to be an edge pixel if any of its eight neighboring pixels did not have the same intensity. Edge pixels were set to black and all other pixels were set to white.

After processing the image as described above and in the previous section, values of D in scaling (1) were determined from linear regression of $\log N(\varepsilon)$ vs. $\log \varepsilon$ and the slope as an estimate of $-D$. The value of ε ranged from a minimum of ε_{\min} pixels to a maximum of ε_{\max} pixels, equal to half the height or width of the image, whichever was shorter. Rather than determining the value of ε_{\min} directly, the scaling was checked over a range of values, $1 \leq \varepsilon_{\min} \leq \varepsilon_{\max}$.

Some results of the analysis for image 5 are plotted in Figs. 8 and 9. Fig. 8 shows the typical behavior of $N(\varepsilon)$ vs. ε on a log–log plot; the slope of this plot is taken to be an estimate of $-D$. Fig. 9 plots the estimates of D for the range of T values and several values of ε_{\min} . We take the plateau in one of these plots — $108 \leq T \leq 255$, here — and then estimate the dimension by taking the mean of D over this plateau and using the standard deviation as an estimate of the error. Each experimental point in Fig. 2 is an average over plateaus in several plots like those in Fig. 9,

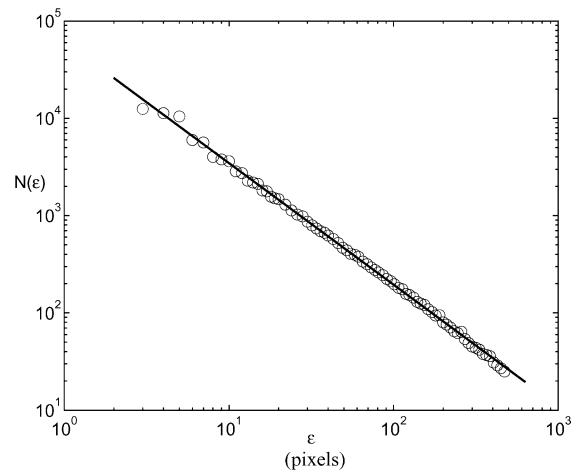


Fig. 8. $N(\varepsilon)$, the number of boxes of size ε needed to cover the boundary vs. ε . The negative of the slope of this graph, 1.28, is taken as an estimate of D , where D is the fractal dimension of the basin boundary in configuration 3, Fig. 5 thresholded at $T = 156$.

each created for different values of ε_{\min} . The error bars are the standard deviation of D over these plots. In configurations 1–4, ℓ (and, thus, α) was determined to 2%, while in configuration 5, the percentage

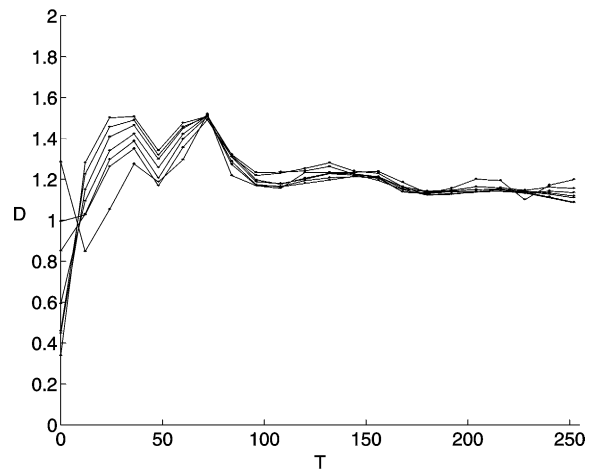


Fig. 9. Dimension estimates at various values of T , the intensity threshold. Each curve represents a different value of ε_{\min} , where $\varepsilon_{\min} \in \{68, 51, 38, 28, 19, 14\}$ pixels. The hump toward the left of the plot corresponds to cases where the boundary is entirely lost in the thresholding process and the image appears noisy. We average over the points in the plateau, $T \geq 108$ (as well as similar plateaus at other values of ε_{\min}), to get a single estimate of the fractal dimension. Such estimates for each configuration are given in Fig. 2.

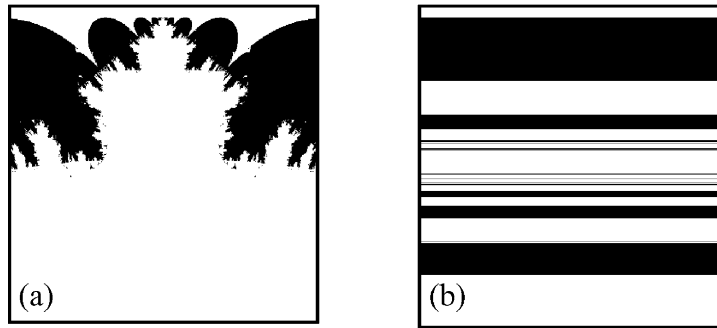


Fig. 10. Basins in a simulation of configuration 3. White (black) points represent initial conditions that exit downward (upward) from the billiard. (a) A patch of initial conditions was chosen on the inward facing surface of one of the raised spheres, call it sphere S (see Fig. 1) each with initial incident direction vector pointing parallel to the line connecting the centers of S and the opposing sphere. (b) Zoom on basin boundary in (a), the fractal dimension of images like (b) were measured for each configuration using the uncertainty dimension technique.

error in ℓ was as small as that in d , the diameter of the balls (much smaller than all other errors in our experiment).

5.2. Simulation

We have performed simulations of these billiard systems to compare with the experimental results. We have found that the basins and their boundaries appear qualitatively similar, and the fractal dimensions determined from the experiment and the simulations agree closely in all five configurations (see Fig. 2).

Fig. 10a shows a two-dimensional slice of the state space of a simulation of configuration 3. A patch of initial conditions was chosen on the inward facing surface of one of the raised spheres, call that sphere S (see Fig. 1) each with initial incident direction vector pointing parallel to the line connecting the centers of S and the opposing sphere. Initial conditions that exit upward are colored black and initial conditions that exit downward are colored white. The basin boundary — the boundary between the two colors — is qualitatively similar to that found in Fig. 5. The fractal dimension of this boundary, as seen in Fig. 10b, and the boundary in similar images for the other four configurations were measured using the uncertainty dimension technique of [8] (a technique which gives the box-counting dimension [16]), see Fig. 2.

6. Possibilities for future study

Optical billiards offer potentially rich ground for future experimental study. As examples, in this section we discuss two other configurations displaying topologies different from those we have studied in Sections 1–5.

6.1. Hairy rings

The configuration we discuss in this section is obtained by starting with configuration 5, and lifting the top sphere up (keeping its center equidistant from the other three spheres). This creates a configuration with two exits, upward and downward through the central hole bounded by the three bottom spheres (Fig. 11). First note that if the top spheres were removed from the scatterer altogether, the three lower spheres would create a basin boundary with dimension 1. Since this boundary set is a closed curve, we refer to it as a “ring”. When the top sphere is returned to its lifted position, the smooth basin boundary ring is reflected in it and the tops of the lower three spheres over and over creating a fractal set that contains infinitely many “hairy rings”, i.e., each point in each ring component of the basin boundary has other parts of the boundary set limiting on it from the exterior of the ring. The points in the image that are outside the rings are in the basin of upward escape. The computer generated plots in Fig. 12 shows the escape times — the number

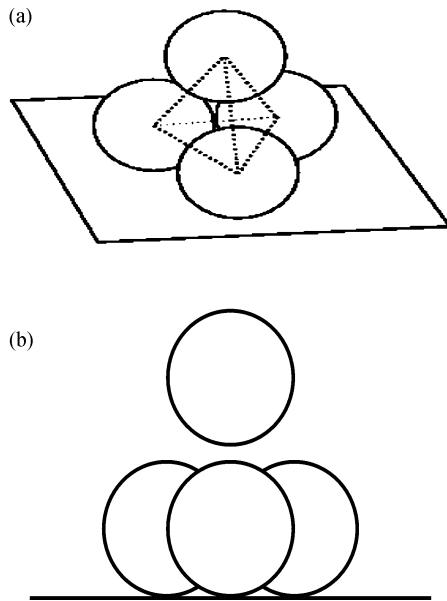


Fig. 11. An alternative optical billiard. (a) Schematic. (b) Front view of (a).

of bounces the orbit experiences before escaping the scattering region — of two sets of initial conditions. (Fig. 12b is a blowout of the boxed region in Fig. 12a.) The intensity of the plotted points increases with the escape time (number of bounces). Note that the union of the interiors of all of the rings is in the basin of downward escape from the scattering region and the rest of the image is in the basin of upward escape. For the case shown in Fig. 12, numerical determination of the basin boundary dimension by the uncertainty dimension technique yields $D = 1.43$.

6.2. Cantor dust

As another example, if we, again, start with configuration 5, but now pull all of the spheres apart so that the distance between any two spheres is the same as in Fig. 13 (i.e., the centers of the spheres are still on the vertices of a regular tetrahedron, but this tetrahedron is large enough so that the spheres are not touching). In this case the surfaces of the spheres do not separate different types of exits. Hence, the dynamics does not define distinct basins. Although there is no basin

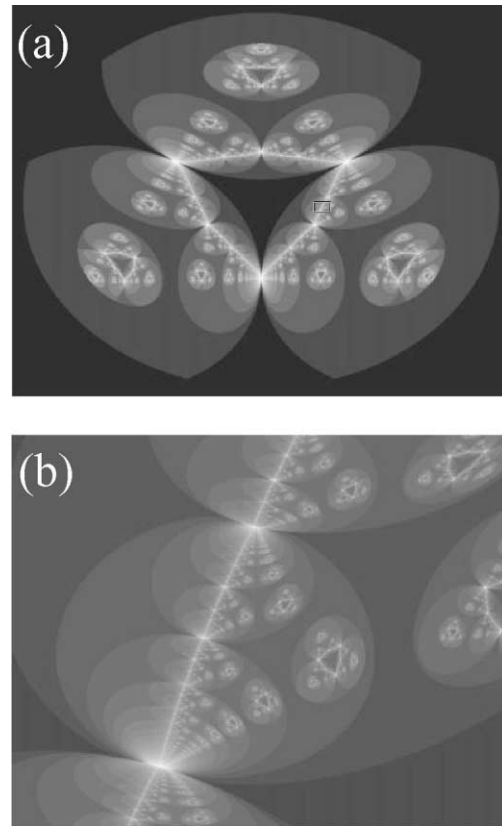


Fig. 12. (a) Escape times for a grid of initial conditions chosen on the bottom surface of the top sphere each with initial incident direction vector pointing straight upward. Brighter points correspond to higher escape times. The points that are on the stable manifold are approximated by the brightest points in the plot. (b) Blow up of box in (a) straddling boundary of large ring.

boundary in this case, there is still a chaotic saddle and its stable manifold, both of which are fractal [6]. This stable manifold appears, in section on the surface of a sphere, as a Cantor dust as shown in the computer generated plot in Fig. 14. (We say a closed set is a Cantor dust if it is fractal and completely disconnected, i.e., no two points in the set can be connected to each other by a curve that does not leave the set.) In Fig. 14 we have colored initial conditions starting on the surface of the top sphere with incident angle directly upward so that the brighter points in the plot correspond to initial conditions that generate orbits that bounce more times before escaping the scatterer (as in Fig. 12). Noting that points in the stable manifold

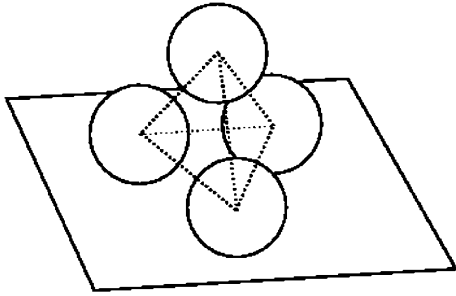


Fig. 13. Schematic of an alternative optical billiard.

bounce an infinite number of times (i.e., never escape the scatterer) and that the map is piecewise continuous (so that points nearer the stable manifold evolve like orbits on the stable manifold for longer times), we see that the plotted points are a good approximation to the stable manifold (in this two-dimensional slice). To experimentally view this stable manifold, one could use the technique used for configuration 5. Initial conditions which are closer to the stable manifold will appear darker (for reasons discussed in Section 4), so thresholding the image could eliminate all but a set of

points approximating the stable manifold. One might expect a better approximation to be had from spheres with higher reflectivity (e.g., spheres with a silver coating) as light could bounce between the spheres more times before reaching to becoming too dark to see, thus, making the darkest regions of the image smaller. With our setup we were unable to get good results for this configuration, possibly because our spheres had a reflectivity that was too low.

6.3. Ellipsoid in a pipe

Surface shapes other than spherical are also of interest. One could potentially fashion a reflective ellipsoid and place it in a vertical reflective rectangular tube with the longest axis of the ellipsoid along the longest axis of the tube to create the billiard studied in [12,13]. The basin boundary in this system is a continuous, nowhere-differentiable surface, but, because of its symmetry about the horizontal midplane of the ellipsoid, its fractal dimension is smaller than the value predicted for typical systems by the conjecture of [17,18]. Tilting the ellipsoid slightly restores agreement with

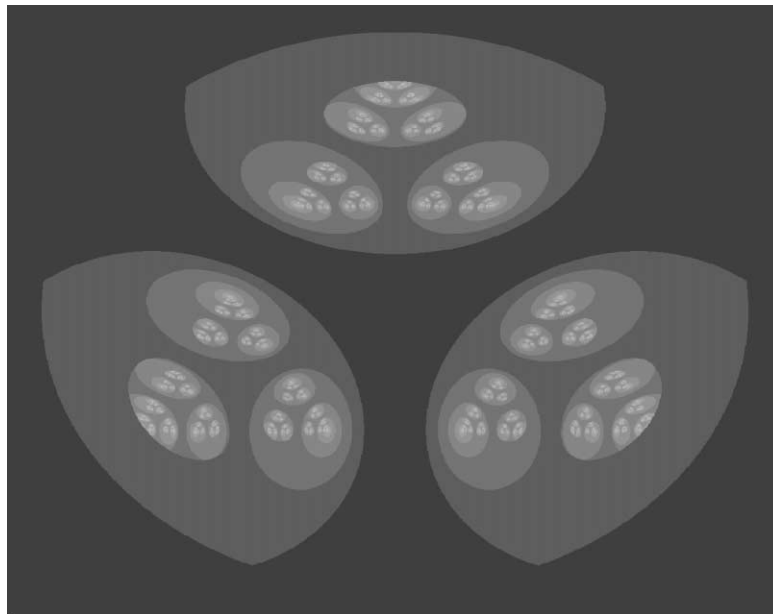


Fig. 14. Escape times for a set of initial conditions chosen as in Fig. 12. Points that are on the stable manifold form a Cantor dust in this two-dimensional slice of the state space. See caption of Fig. 12 for more details.

this formula [12,13]. This effect could be studied experimentally using the techniques discussed above.

6.4. Decay time

Finally, one might measure quantities describing these systems other than the fractal dimension. One quantity of importance in the study of chaotic scatterers is the characteristic decay time τ : sprinkle a large number of initial conditions in a region intersecting the stable manifold of the chaotic saddle. After $n \gg 1$ reflections, the number of orbits remaining in a finite-sized region containing the entire chaotic saddle decays like $\exp(-n/\tau)$. This defines the decay time τ . One important aspect of this quantity is that it is conjectured to be related to the fractal dimension [17,18]. The decay time could be measured experimentally by sending short (picosecond) laser pulses into the scatterer. The amount of light escaping the scatterer at times shortly after the pulse should decay exponentially with characteristic time τ .

7. Conclusion

Optical billiards offer a convenient way of experimentally studying and gaining intuition for chaotic scattering systems. We have described experimental techniques for measuring the fractal dimension of basin boundaries and other stable manifolds, observed basin boundaries having two distinct topologies, and found that fractal dimension measurements agree well with simulation.

The optical billiards we have studied possess basin boundaries that are either continuous, nowhere-differentiable surfaces, or are Wada boundaries. The images in Figs. 4–6 represent the first experimental observations of the continuous, nowhere-differentiable surface topology, and Fig. 7 represents the first experimental study of Wada boundaries. Likewise, Fig. 2 shows the results of the first experimental measurements taken on these types of boundaries.

Basin boundaries for chaotic scatterers in three-dimensional space can be readily visualized and studied. A few reflective surfaces may be easily manipulated into various configurations and the geometry changed as the viewer changes the positions, orientation, and lighting of the scatterers. This sort of experimentation can be performed at any desk, e.g., with four silver Christmas tree ornaments, but data taking may require special surfaces. (In fact, commercially available Christmas ornaments are silver coated on the *interior* of a hollow, glass sphere leading to reflections from both the inner and outer surfaces.)

We believe that optical billiards offer an opportunity for interesting future study. In Section 6 we mention some possible candidates for future investigation, although there are surely many others.

Acknowledgements

This work was supported by the Office of Naval Research (Physics) and NSF DMR-9896037. Daniel P. Lathrop is a Cottrell Scholar of the Research Corporation. We thank James A. Yorke for helpful discussions.

References

- [1] Z. Kovacs, L. Wiesenfeld, Phys. Rev. E 51 (1995) 5476.
- [2] P.T. Boyd, S.L.W. McMillan, Chaos 3 (1993) 507.
- [3] N.J. Cornish, E.P.S. Shellard, Phys. Rev. Lett. 81 (1998) 3571.
- [4] J. Levin, Phys. Rev. Lett. 84 (1999) 3515.
- [5] J.C. Sommerer, H.-C. Ku, H.E. Gilreath, Phys. Rev. Lett. 77 (1996) 5055.
- [6] Q. Chen, M. Ding, E. Ott, Phys. Lett. A 115 (1990) 93.
- [7] D. Sweet, E. Ott, J.A. Yorke, Nature 399 (1999) 315.
- [8] E. Ott, Chaos in Dynamical Systems, Cambridge University Press, Cambridge, 1993 (Chapter 5).
- [9] S.W. McDonald, C. Grebogi, E. Ott, J.A. Yorke, Physica D 17 (1985) 125.
- [10] J.P. Cusumano, B.W. Kimble, Nonlinear Dynam. 8 (1995) 213.
- [11] J.F. Heagy, T.L. Carroll, L.M. Pecora, Phys. Rev. Lett. 73 (1994) 3528.
- [12] D. Sweet, E. Ott, Phys. Lett. A 266 (2000) 134.
- [13] D. Sweet, E. Ott, Physica D 139 (2000) 1.
- [14] T. Harayama, P. Davis, Opt. Lett. 23 (1998) 1426.
- [15] H.E. Nusse, J.A. Yorke, Science 271 (1996) 1376.
- [16] S. Pelikan, Trans. Am. Math. Soc. 292 (1985) 695.
- [17] B.R. Hunt, E. Ott, J.A. Yorke, Phys. Rev. E 54 (1996) 4819.
- [18] M. Ding, E. Ott, Ann. NY Acad. Sci. 751 (1995) 182.